

EXPLORING THE RADIO SKY FOR NATURAL AND ARTIFICIAL TRANSIENT SOURCES

ASSOC. PROF. EVAN F. KEANE
ASTROPHYSICS RESEARCH GROUP

OWEN A. JOHNSON BSC.
TRINITY COLLEGE DUBLIN, 2026

Trinity College Dublin

Coláiste na Tríonóide, Baile Átha Cliath

School of Physics



*For my parents, who sacrificed so much,
so I could chase the stars.*

Declaration

I hereby declare that this thesis is entirely my own work and that it has not been submitted as an exercise for a degree at this or any other university.

I have read and I understand the plagiarism provisions in the General Regulations of the University Calendar for the current year, found at <http://www.tcd.ie/calendar>.

I have also completed the Online Tutorial on avoiding plagiarism 'Ready Steady Write', located at <http://tcd-ie.libguides.com/plagiarism/ready-steady-write>.

I agree to deposit this thesis in the University's open access institutional repository or allow the library to do so on my behalf, subject to Irish Copyright Legislation and Trinity College Library conditions of use and acknowledgement.

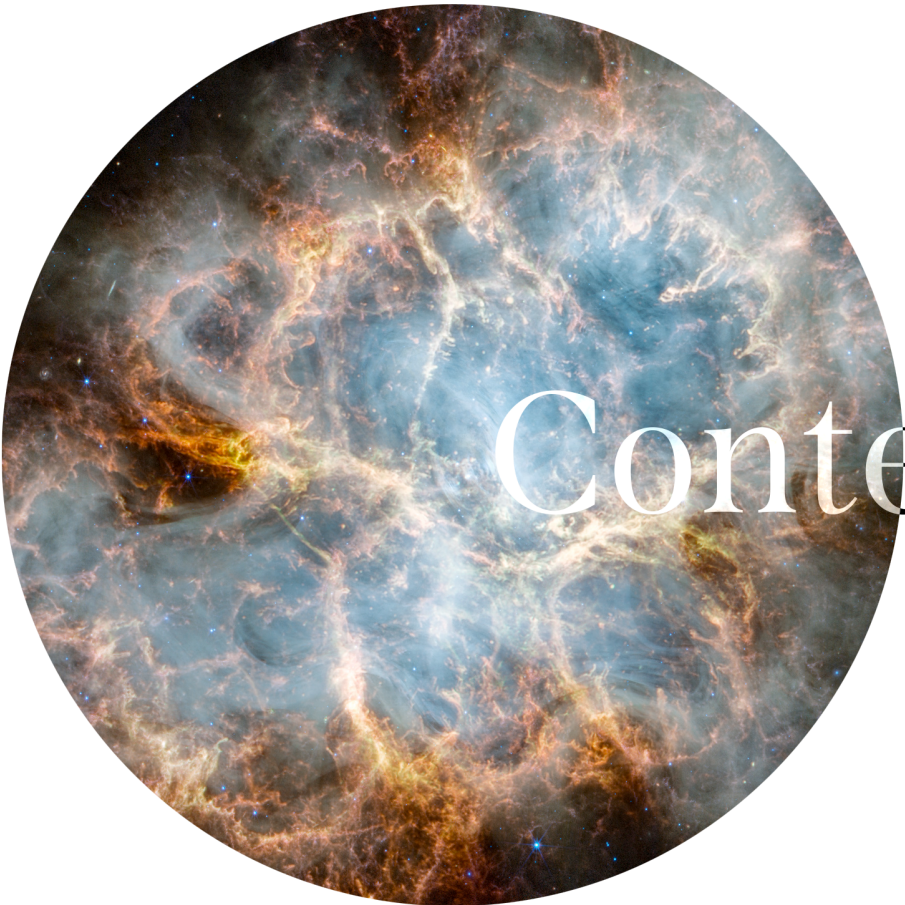
Signed: _____

Date: _____

This is some text to be centered vertically.

Abstract

Fortunately there are still many open questions about this wild and wondrous cosmos that we find ourselves in.



Contents

1	Introduction	1
1.1	Background	1
2	Dual-site Technosignature Searches	3
2.1	Introduction	3
2.1.1	Scientific Motivation	3
2.1.2	Breakthrough Listen	4
2.2	Observations	4
2.2.1	LOFAR	5
2.2.2	Targets	5
2.2.3	Simultaneous observations	6
2.3	Analysis	9
2.3.1	Barycentric correction	10
2.3.2	Searching for Narrowband Signals	10
2.3.3	Dual-site coincidence rejection	11
2.3.4	Search Results	12
2.4	Discussion	13
2.4.1	Survey Sensitivity	13
2.4.2	Starlink Interference	14
2.4.3	Figure of Merit	15
2.4.4	110 - 190 MHz Technosignature Parameter Space	16
2.4.5	Future work using LOFAR 2.0	16
2.5	Conclusion	17
A	Useful Formula	21
A.1	Fundamentals	21
A.2	Radiometer	21
A.3	Pulsars	21
A.3.1	Spin Down	21
A.4	Binary Pulsars	21
A.5	Dispersion Measure	21
A.6	Units	21
B	Post-detection Barycentric Correction	23
B.0.1	Algorithm outline	23
B.1	Sensitivity of the Survey across the HBA	24

List of Figures

2.1	An Aitoff projection of the sky in Galactic coordinates depicts the distribution of survey pointings, with the Galactic disk shaded in grey. <i>Gaia</i> sources are omitted from the plot due to their extremely high source density. Grey dots represent <i>TESS</i> Targets of Interest (ToIs). Those targets observed during our survey are marked with red dots at boresight with green showing the half-power beam width (2.59°).	4
2.2	This figure illustrates one of the boresight pointings directed at a <i>TESS</i> object (highlighted in green), with the LOFAR beam's Full-Width Half-Maximum (FWHM) shown in pink. The background image is from the Sloan Digital Sky Survey (?; SDSS).	6
2.3	A Hertzsprung-Russell diagram of the 1,631,198 <i>Gaia</i> targets searched for technosignatures in this survey with a mean distance of 1270 pc. The relative distribution with respect to spectral type is: O < 0.01%, B—0.4%, A—6.94%, F—11.01%, G—31.56%, K—47.84%, M—2.12%. This is as opposed to the general <i>Gaia</i> catalogue which is: O, B < 0.0001%, A—1.5%, F—18.9%, G—44.4%, K—34.5%, M—0.6%.	7
2.4	The LOFAR HBA beam's sensitivity at 150 MHz changes in relation to the off-axis boresight angle (θ). Furthermore, a plot of the number of filtered <i>Gaia</i> targets within the beam pointing as a function of θ is presented. The \times represents the value for the Full Width Half Max of the beam.	8
2.5	iLiSA block diagram, showing how an operator-defined schedule is ingested and is executed in a timely fashion. Data then begins to flow and ends up being ingested by processing pipelines together with associated metadata.	8
2.6	Comparison of drifting signals or ‘hits’ detected at both stations seen across the HBA frequency band. Each bin within the data set represents a 1 MHz frequency range and is accompanied by a corresponding percentage indicating its proportion to the overall data set.	9
2.7	A scatter plot of the drift rate values against detected frequency. The Irish station is shown in pink and the Swedish station is shown in blue.	10
2.8	Dynamic spectra (waterfall plots) of detected narrow-band signal centered on the detected frequency of detection, showing the two most common cases of coincidence rejection. Case A (<i>left</i>) shows a narrowband signal with a non-zero drift rate detected at I-LOFAR and not LOFAR-SE. Case B (<i>Right</i>) shows the opposite where a non-zero drift rate signal is not detected by I-LOFAR but is detected by LOFAR-SE. For a signal to be considered a detection of interest both sites would have to exhibit non-zero drift rate signal at the same frequency simultaneously.	11
2.9	The <i>top</i> two plots represent narrowband signals detected at both stations in the topocentric frame of reference. The <i>bottom</i> two plots show the same detected narrowband signals detected at both stations but corrected to the barycentric frame of reference. This is illustrated by the newly added drift to signals present in the post correction.	12
2.10	Cumulative histogram of EIRP limits of this survey across the HBA band. Reference luminosities for three civilization levels emitting 10^{17} , 10^{13} or 10^{10} W are shown in blue, red and green respectively. The percentage of targets where the station is sensitive to the transmission of 10^{17} W is shown, as a function of frequency across the band. At lower frequencies sensitivity to 10^{17} emitters drops off as the T_{sys} rises. The \bar{T}_{sys} varies from 1260 K down to 322 K as frequency is increased across the band. Detailed calculations are presented in Appendix B.	14

2.11 Comparison of our study (highlighted in red) to prior surveys. The plot presents the transmitter rate versus Effective Isotropic Radiated Power (EIRP), with the grey line indicating the transmitter rate as a function of EIRP. A solid vertical grey line illustrates the energy surplus of a Kardashev Type-I civilization. Additionally, a dotted-dashed grey line depicts the EIRP of the Arecibo planetary radar. The gray thick line shows the slope of the transmitter-rate as a function of their EIRP power. Distance used for EIRP calculation is $\bar{d} + d_\sigma = 7009$ ly.	15
2.12 The fraction of stars that produce narrow-band emission (f_c^n) against the transmitter power of the total target pool. The hashed region (red) shows the constraints this survey places on a value of f_c^n at 110 - 190 MHz.	16
B.1 Doppler drift of a narrowband signal in the topocentric observing frame at four different observing epochs. Simulated waterfalls with narrowband signals observed from the Irish LOFAR station towards the direction of TIC 27677846 are shown for different times of the year in blue. The expected sign and direction of change of the relative velocity are labeled at the top of each plot. It is assumed that a hypothetical narrowband ETI signal is transmitted at a constant frequency of 1420 MHz (with zero drift rate). As shown, the same signal is observed at different frequencies and drift rates depending on the sign and direction of change of the relative velocity at different epochs of observations. For instance, in the first panel, the relative velocity is positive and increases with observing time. Therefore, the observing frequency has been shifted to a lower frequency (as described by Equation 2.3.1), and it continues to shift to even lower frequencies with time.	23
B.2 A typical filterbank file stores data in a time and frequency matrix format. Each row represents a sample, while each column represents a frequency channel for a given sample. Time is increasing from bottom to top while the frequency is increasing from right to left.	24
B.3 These plots depict the expected spectra at their respective barycentric frequencies and the spectra after the correction for barycentric relative velocity. Each plot represents a single spectrum, where the frequency increases from right to left. (a) In the case of $+v_{rel}$, the first channel of the topocentric spectra is shifted to a higher barycentric frequency compared to the last topocentric spectra channel, which causes an expansion of the spectra. If two consecutive channels move farther away from each other (shown as f_1 and f_2) by more than half the channel width, an additional channel is added in between, which is the summation of these two channels. Extra channels at the edge of the spectra are dropped. (b) In the case of $-v_{rel}$, the first channel of the topocentric frequency is shifted to a lower barycentric frequency relative to the last topocentric spectra channel, which causes a squeeze in the spectra. If two consecutive frequency channels shift closer to each other by more than half a channel width, these channels are added together and an extra channel is added at the end containing zeros. The bottom spectra in each plot illustrate these expansion and squeeze effects after correction are applied from the code.	25
B.4 An outline of the post-detection barycentric correction algorithm for an input filterbank file in <code>sigproc</code> format. For this case, the input filterbank file has a descending order in frequency, and v_{rel} represents the relative velocity between the transmitter and observer. The algorithm considers two cases depending on whether the relative velocity is positive or negative, which indicates whether the source is moving away from or towards the observer, respectively. Each of these cases is further divided into two where the absolute value of the relative velocity can either increase or decrease, requiring the spectra to be shifted to either the higher or lower frequency end. For all cases with $+v_{rel}$, each spectra is expanded, and for $-v_{rel}$, each spectra is squeezed, as shown in Figure B.3. The code then writes each of these spectra into another <code>sigproc</code> filterbank file, which will have each channel frequency closely corrected to the barycentric frame of reference.	26

List of Tables

2.1	Specifications for the data input to our processing pipeline after pre-processing and preparing the raw data with <code>udpPacketManager</code> (McKenna et al., 2023).	9
2.2	Comparison of the number of narrow-band signals detected for a subset of <i>TESS</i> objects in both the topocentric and barycentric reference frame. <code>turboSETI</code> searches were completed using identical parameters in each reference frame. A small number of mutual hits were found in the topocentric frame, but these were filtered out entirely in the barycentric case.	11
2.3	<i>TESS</i> candidates used as bore sight pointings for the survey. These targets were selected from the NASA Exoplanet Archive (NEA) based on visibility at both LOFAR stations.	13
2.4	<i>Gaia</i> candidates found within 1.295° of <i>TESS</i> boresight pointings. The <i>Gaia</i> target pool is drawn from GDR3. Filtering was applied based on parallax error; targets with distance errors $> 20\%$ were excluded to preserve EIRP sensitivity.	13
B.1	Statistics on sensitivity across the HBA band. The K1 and Earth detectable values represent the percentage of the target sample that are detectable.	25

Nomenclature

1 | Introduction

“the Universe, she’s whispering so softly I can hear all. The croaking insects, all the taxicabs, all the bum’s spent change All the boys playing ball in the alleyways”
— Gregory Alan Isakov, *The Universe*

1.1 Background

2 | Dual-site Technosignature Searches

“The universe is a pretty big place. If it’s just us, seems like an awful waste of space.”
— Carl Sagan, *Contact*

2.1 Introduction

In the last 50 years, evidence has steadily mounted, that the constituents and conditions necessary for life are common in the Universe (?). Predicting specific properties of electromagnetic emissions from extraterrestrial technologies is one of the most challenging aspects of searching for life in the universe. However, it also represents a high-risk, high-reward endeavor. If an extraterrestrial civilization were intentionally attempting to indicate its presence through such emissions, it would be advantageous to make the signals easily distinguishable from natural phenomena. The evidence of such emissions is referred to as ‘technosignatures’, and the field dedicated to their detection is known as the Search for Extra-terrestrial Intelligence (SETI).

It is commonly assumed that civilizations elsewhere in the universe may employ similar technologies to those developed on Earth. Consequently, radio frequencies are considered a logical domain for conducting SETI surveys due to the widespread use of telecommunications and radar. Therefore, radio astronomy has played a significant role in the field of SETI since the 1960s (??). Numerous previous SETI surveys have utilized large single dish telescopes operating at frequencies $\gtrsim 1\text{ GHz}$ (Tarter, 1996; Siemion et al., 2013; ?) ¹. However, exploration of the radio window below 1 GHz has been relatively limited. Technosignature searches commonly seek narrowband (approximately Hz-scale) radio emissions, either transmitted directly or leaking from other civilizations. Nonetheless, there is no inherent preference for any specific segment of the radio spectrum, which necessitates surveys spanning from low frequencies (30 MHz) to high frequencies (100 GHz; ?). At 30 MHz it becomes very difficult to observe from the ground due to ionospheric conditions (see ?, chap. 7.8). This study primarily focuses on low-frequency SETI in the 110 - 190 MHz range.

2.1.1 Scientific Motivation

Low-frequency radio SETI presents significant challenges due to higher sky temperatures, which limit the sensitivity of the underlying observations. The Murchison Widefield Array (MWA, ?) in Western Australia has been at the forefront of low-frequency SETI research thus far (???). However, the LOw Frequency ARray (LOFAR) presents a compelling scientific case for conducting a SETI survey (?). Aside from operating at low frequencies in the northern sky, LOFAR offers a large field of view, enabling the search for technosignatures across thousands of stars in each observation.

Radio SETI also grapples with the challenge of handling a significant amount of radio frequency interference (RFI). Traditionally, SETI surveys have been conducted using single dish radio telescopes. While these telescopes offer operational convenience and room for upgrades, they possess limitations in effectively distinguishing between sources of interference and authentic sky-bound signals unless equipped with multibeam receivers. In contrast, the utilization of two local LOFAR stations presents two notable advantages over conventional single dish surveys. As demonstrated in studies conducted by ? and ?, single dish surveys typically employ an ‘ON’ and ‘OFF’ observing technique, where the target is observed

¹See ? for a review

for five minutes ('ON') followed by five minutes of observing a different location ('OFF'). This cycle is repeated three times, resulting in three 'ON' pointings and three 'OFF' pointings. This approach facilitates the identification and elimination of narrowband signals detected in the local environment that could potentially interfere with the search for technosignature candidates. By employing multiple stations, the search benefits from the unique local RFI environments at each station. This leads to a higher rate of rejecting false positive signals compared to the aforementioned surveys, which have signals of interest on the order of thousands. Additionally, since there are two stations involved, there is no requirement to alternate between an 'ON' and 'OFF' observation regime. As a result, the entire observation duration can be dedicated to directly observing the target, as the comparison of RFI environments would yield the same effect. This characteristic renders SETI surveys with two or more telescopes a highly valuable resource, particularly in today's RFI environments.

2.1.2 Breakthrough Listen

The Breakthrough Listen (BL) program is conducting one of the most comprehensive searches for evidence of intelligent life by extending the search to a wide variety of targets from existing ground-based observing facilities (see ? for a review). All of the existing observations within the BL program have so far been conducted in the 1 – 27.45 GHz range (?).

In this paper we report on low frequency extension of the BL initiative using two international LOFAR stations to perform simultaneous dual-site observations of nearby exoplanet candidates of interest from both the Transiting Exoplanet Survey Satellite (*TESS*; ?) and from *Gaia* (?) in collaboration with the BL program. This survey also demonstrates the proof of concept of using dual-site observations for the rejection of spurious local sources of terrestrial origin. This method thus removes the need for separate 'ON' and 'OFF' pointings (?). In § 2.2 we describe the observational set up and the data acquired. § 2.3 explains the data analysis steps taken. We discuss the implications of this work in § 2.4 before concluding in § 2.5.

2.2 Observations

This study encompasses a total of 44 targeted pointings, where each pointing consists of a 15-minute scan centered on specific targets selected from the *TESS* catalog, focusing on confirmed or candidate exoplanets (refer to Figure 2.1). The entire observation campaign spanned a duration of 11 hours, covering an area of 232 deg² in the northern sky.

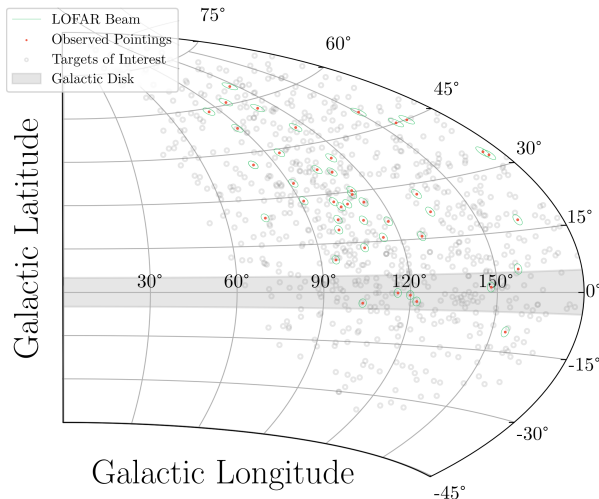


Figure 2.1: An Aitoff projection of the sky in Galactic coordinates depicts the distribution of survey pointings, with the Galactic disk shaded in grey. *Gaia* sources are omitted from the plot due to their extremely high source density. Grey dots represent *TESS* Targets of Interest (ToIs). Those targets observed during our survey are marked with red dots at boresight with green showing the half-power beam width (2.59°).

2.2.1 LOFAR

LOFAR, a pioneering low-frequency aperture array telescope, spans hundreds of kilometers across Europe and serves as a pathfinder to the Square Kilometer Array (SKA). The array consists of a core station with outrigger stations situated in the Netherlands and additional international stations spanning multiple countries, such as Germany, France, Sweden, Ireland, Latvia, Poland, and the United Kingdom. Additionally, stations are currently in the process of being constructed in Italy and Bulgaria. The LOFAR array operates using two types of antenna, the Low Band Antenna (LBA) and the High Band Antenna (HBA), operating at 10-90 MHz and 100-250 MHz respectively. In this study, the HBAs at the Irish and Swedish LOFAR station are used to carry out observations non-interferometrically. The field-of-view (FoV) of an international LOFAR station is rather large; at full-width-half maximum it is 5.3, 3.4 and 2.3 deg² at frequencies of 120, 150 and 180 MHz, respectively (?). With such a large region where our observations are sensitive, each pointing contains millions of stars that can be searched for technosignatures ([Włodarczyk-Sroka et al., 2020](#)). In this survey, in addition to the 44 *TESS* targets at boresight, 1,631,154 *Gaia* targets are covered by our observations and so are searched for technosignatures.

2.2.2 Targets

A significant fraction of radio emission from Earth is emitted in the direction of the ecliptic plane. For example, powerful planetary radars are used to explore solar system objects ([Siemion et al., 2013](#)) and high-powered transmitters are used to communicate with solar system probes (?). It is conceivable then that such leakage radiation may also be emanating from other worlds, preferentially in *their* planetary orbital planes. This is why we chose *TESS* targets, as these are the closest transiting exoplanet systems known (??). Observing these sources with the LOFAR HBAs enables robust constraints on any associated artificial low-frequency radio emission.

TESS Targets

In order to determine a target list for this work, the latest list of *TESS* object of interests (TOIs) was retrieved (?) and a shortlist of targets were obtained rejecting possible false positives. Since the sensitivity of the HBA array is best ±30° of zenith, the required overlap for both LOFAR international stations spans the declination range +27° to +83°. Further practical considerations were also accounted for, i.e. to stay as far from bright sources like the Sun as possible at both sites, and to balance sensitivity at both sites (?)². We report observations towards 44 unique targets from the *TESS* catalogue in this study, where each target was observed for 15 minutes. Figure 2.1 shows the distribution of these targets observed in comparison to the pool of all *TESS* TOIs.

Gaia Sources

The beam of a LOFAR station has an expansive coverage enabling observation of a substantial number of stars in the field-of-view. The significance of these in-field stars has been highlighted by [Włodarczyk-Sroka et al. \(2020\)](#). Consequently, during our observations targeting 44 sources from the *TESS* catalogue, we encountered a significant number of in-field stars within our field-of-view as shown in Figure 2.2.

To determine the list of targets within this field-of-view, we utilized the *Gaia* catalogue. Some previous major SETI surveys focused their searches towards Sun-like stars ([Tarter, 1996](#)). However, since our understanding of the origin of life is limited, it makes sense to allow for the possibility of life arising on a planet that is neither Earth-like, nor around stars that are Sun-like. Similarly, we should consider planets not necessarily located in the habitable zone. This is typically characterized as the orbital range wherein liquid water could exist (?), as inferred from planetary equilibrium temperatures often ignoring the unknown albedo of the exoplanets. Any sensitive radio SETI survey seeking to maximize the chance of detecting weak radio signals should, insofar as possible, expand its search to encompass nearby stars of a broad range of spectral types and with exoplanets of all sizes and distances from their parent star. Thus, we conducted calculations to determine the number of *Gaia* stars with a mean distance of 1215 pc, with an accuracy in their distances of at least 20%.

This study used *Gaia*'s third data release (GDR3; [?Ginsburg et al., 2019](#)). When analyzing GDR3 two filters were applied to the in beam target values survey volume and sensitivity accuracy. Firstly a

²These selection criteria were applied using a custom developed dual-site observation planning software.

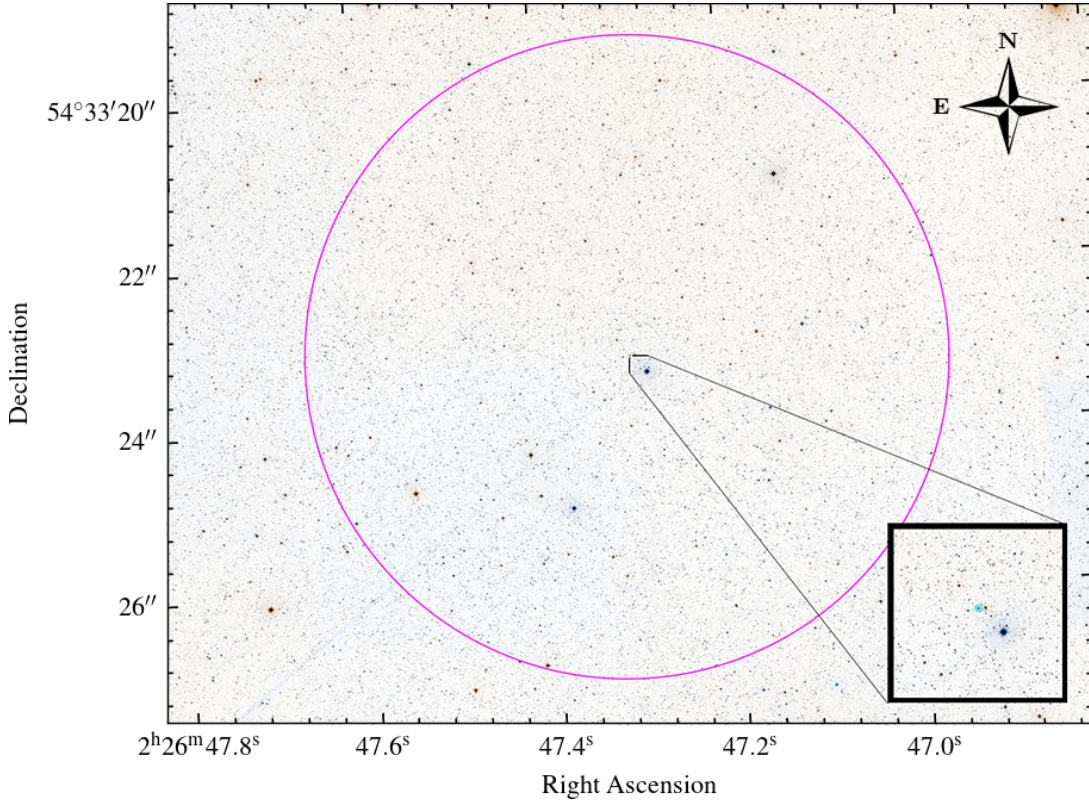


Figure 2.2: This figure illustrates one of the boresight pointings directed at a *TESS* object (highlighted in green), with the LOFAR beam’s Full-Width Half-Maximum (FWHM) shown in pink. The background image is from the Sloan Digital Sky Survey (?; SDSS;).

constraint on the RA and DEC errors were implemented. If a *Gaia* source was found to be in the beam but had a error magnitude greater than the FWHM it was removed from the source pool. Equation (2.2.1) states the first condition of filtering.

$$\theta_{\text{sep}} + \sqrt{\Delta\text{RA}^2 + \Delta\text{DEC}^2} < 1.295^\circ \quad (2.2.1)$$

As the sensitivity of the survey is calculated based on a source’s distance a second filter is implemented to remove sources that have large errors. By taking the difference ($\Delta\sigma_G$) in the upper and lower confidence levels of GSP-Photometry³ to obtain a percentage error on distance. All sources with a d_{M_G} error of 20% or greater are filtered out of the source list. Equation (2.2.2) states the second condition of filtering:

$$\frac{\Delta\sigma_G}{d_{M_G}} < 20\% \quad (2.2.2)$$

A total of 1,631,154 stars from this list, making it one of the largest samples of stars ever surveyed for SETI purposes. Figure 2.3 shows a Hertzsprung-Russell diagram for the targets.

2.2.3 Simultaneous observations

Typically, international LOFAR stations operate as standalone telescopes 2 – 3 days per week, i.e. they do not operate as part of the International LOFAR Telescope’s Europe-wide array. This project was undertaken during this standalone time. For this purpose the *international LOFAR in Stand-Alone mode* (*iLiSA*) package⁴ is used to control both telescopes simultaneously. *iLiSA* provides a high-level operational control of multiple LOFAR stations, including scheduling, processing pipeline dispatching and metadata aggregation (see Figure 2.5). For the observations in this study, an operator-produced list of targets that were close⁵ to the local meridian was fed into *iLiSA* at each epoch. Towards each target,

³SQL Keys: `distance_gspphot`, `distance_gspphot_upper` (d_{M_G}) and `distance_gspphot_lower`

⁴<https://github.com/2baOrNot2ba/iLiSA/releases/tag/v6.1>

⁵In practice as Birr and Onsala are separated by ~ 20 deg of longitude, the optimum scheduling is to observe $\sim 40 \text{ min} - T_{\text{obs}}/2$ ‘late’ at Onsala and $40 \text{ min} + T_{\text{obs}}/2$ ‘early’ at Birr.

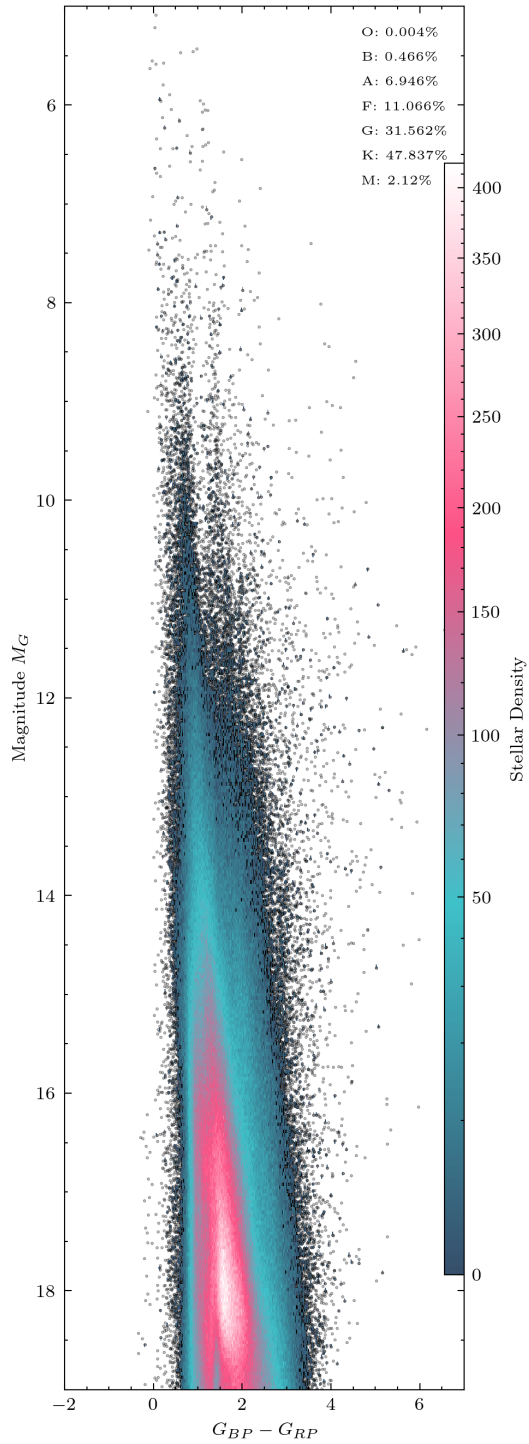


Figure 2.3: A Hertzsprung-Russell diagram of the 1,631,198 *Gaia* targets searched for technosignatures in this survey with a mean distance of 1270 pc. The relative distribution with respect to spectral type is: O < 0.01%, B—0.4%, A—6.94%, F—11.01%, G—31.56%, K—47.84%, M—2.12%. This is as opposed to the general *Gaia* catalogue which is: O, B < 0.0001%, A—1.5%, F—18.9%, G—44.4%, K—34.5%, M—0.6%.

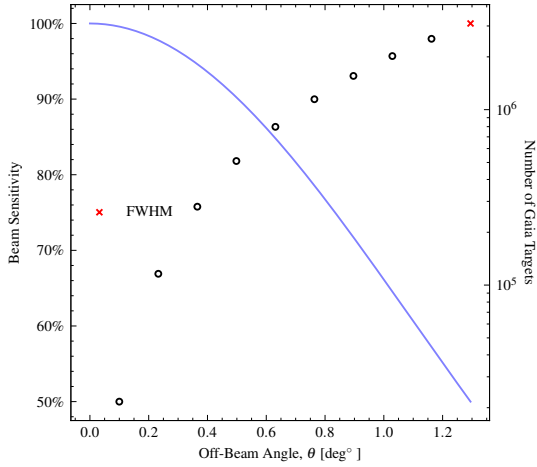


Figure 2.4: The LOFAR HBA beam’s sensitivity at 150 MHz changes in relation to the off-axis bore-sight angle (θ). Furthermore, a plot of the number of filtered *Gaia* targets within the beam pointing as a function of θ is presented. The \times represents the value for the Full Width Half Max of the beam.

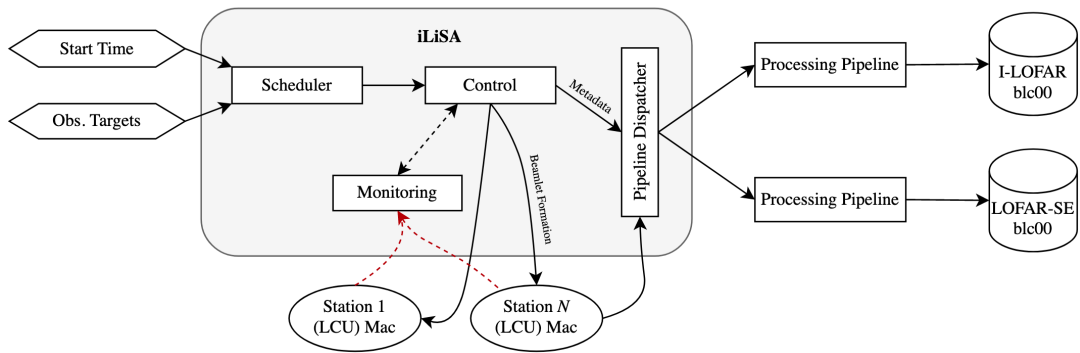


Figure 2.5: iLiSA block diagram, showing how an operator-defined schedule is ingested and is executed in a timely fashion. Data then begins to flow and ends up being ingested by processing pipelines together with associated metadata.

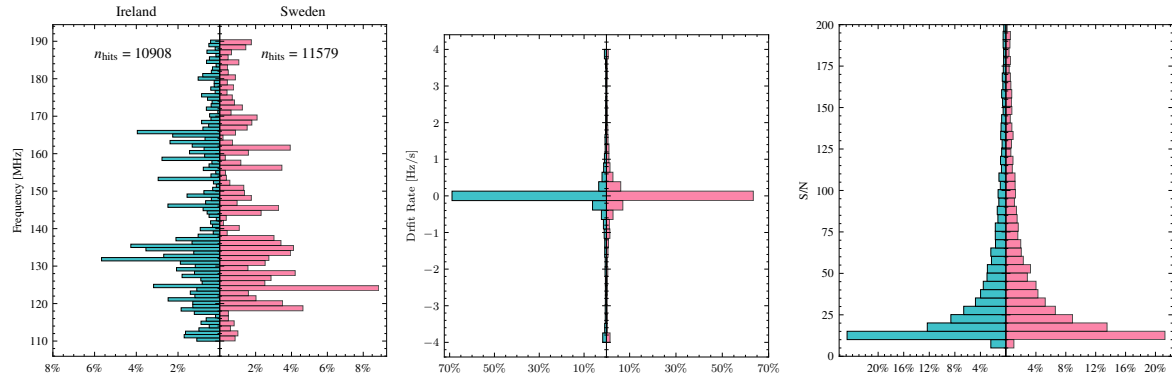


Figure 2.6: Comparison of drifting signals or ‘hits’ detected at both stations seen across the HBA frequency band. Each bin within the data set represents a 1 MHz frequency range and is accompanied by a corresponding percentage indicating its proportion to the overall data set.

one beam per station was formed using `iLiSA`, and each beam was formed with 412 HBA sub-bands (corresponding to a bandwidth of 80.46875 MHz). The scan time on each target was 15 min, and the whole scheduling block was a few hours per epoch.

In this study, the only `iLiSA` pipeline used was the raw data recorder, which simply receives UDP packets of beam-formed data and writes them to disk, separately at each site. The data consist of coarse-channelised complex voltages. The initial data stream is two polarization’s from each antenna. With real Nyquist-sampling with a 200-MHz clock, with a coarse channelisation factor of 512 taking place, only 488 (244) of these being recordable when the data are written as 8-bit (16-bit) complex numbers. Further processing of these data is necessary and we use `udpPacketManager` (McKenna et al., 2023) to ultimately create total intensity `sigproc` (?) formatted filterbank files at the time and frequency resolution appropriate for our Doppler-drift search, shown in Table 2.1.

Data Attribute	Value
Frequency Start (f_{start})	109.9609375 MHz
Frequency End (f_{end})	190.0390625 MHz
Frequency Resolution	2.980232239 Hz
Channel Number	27000832
Obs. Length (t_{obs})	15 mins
Temporal Resolution	0.67108864 s
Maximum Drift Rate Search	$\pm 4 \text{ Hz s}^{-1}$
S/N _{min} threshold	10

Table 2.1: Specifications for the data input to our processing pipeline after pre-processing and preparing the raw data with `udpPacketManager` (McKenna et al., 2023).

2.3 Analysis

The most common transmissions sought in SETI searches are narrow-band (\sim Hz) radio signals. Ubiquitous in early terrestrial communication systems, such signals can be produced with relatively low energy and traverse the interstellar medium easily. They can be readily distinguished from natural astrophysical sources. These signals could either be transmitted intentionally or arise as leakage from extra-solar technologies. The apparent frequency of a distant narrow-band transmitter is expected to exhibit Doppler drift due to the relative motion between the transmitter and receiver. The Breakthrough Listen group has developed an efficient narrow-band search software package which includes a search for such drifting signals, named `turboSETI` (?) which we use for the analysis of our LOFAR survey data. However, before we can compare narrowband signal hits detected using this tool, it was necessary to compare them in the Barycentric reference frame.

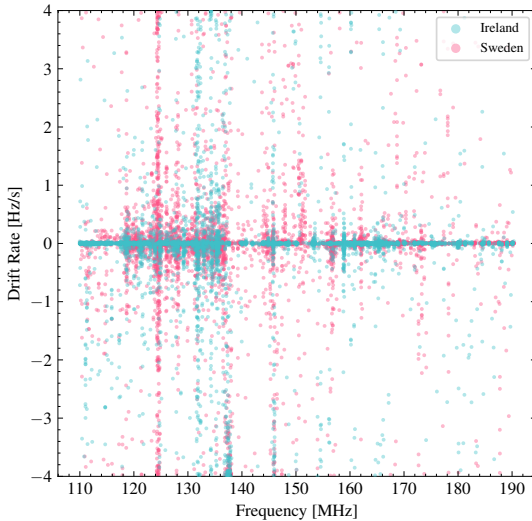


Figure 2.7: A scatter plot of the drift rate values against detected frequency. The Irish station is shown in pink and the Swedish station is shown in blue.

2.3.1 Barycentric correction

The movement of the Earth around its axis and the Sun introduces a Doppler effect that causes radio signals' frequency and arrival time to shift, as

$$f_{obs} = f_{em} (1 - v_{rel}) . \quad (2.3.1)$$

Here, f_{obs} is the observed frequency, f_{em} is the emitted frequency (or barycentric frequency), and v_{rel} is the velocity of the source relative to the observer, normalized by the speed of light. The Doppler effect only depends on the velocity of the source relative to the observer, and for a source moving towards the observer, we can consider $-v_{rel}$, while for a source moving away from the observer, we consider $+v_{rel}$. The relative velocity between the observer and the source will differ for different observing epochs, the location of the source in the sky, and the geographical location of the telescope. For instance, the target TIC 27677846 was observed on UT 2021 July 15, from both the LOFAR stations simultaneously. The expected relative velocity (v_{rel}) towards the source was -7.669×10^{-5} and -7.496×10^{-5} , causing a relative shift ($f_{em} - f_{obs}$) of $+11.504$ kHz and $+11.246$ kHz for a hypothetical ETI signal transmitted at a constant frequency of 150 MHz observed at the Sweden and Ireland stations, respectively. These are significant shifts that are distinct at the two stations, and they need to be corrected to compare the same signal observed at the two stations.

Typically, barycentric corrections are introduced by adjusting the local oscillator during observations. However, in our study, we record beamformed baseband voltages during observations and produce three different data products with varying temporal and spectral resolutions during post-processing (Lebofsky et al., 2019). We are interested in searching for a wide variety of signals, including narrowband signals, broadband transient signals, and wide-band pulsating signals. Introducing local oscillator shifts during observations can impact our other signal searches. Therefore, we correct for barycentric drift after the channelization and detection of the baseband voltages for narrowband signal searches using software which we have developed⁶. Details of this correction and code (?) are fully discussed in Appendix B. For comparison both topocentric and barycentric data are analysed for a small sub-set of the targets and the results are shown in Table ??.

2.3.2 Searching for Narrowband Signals

Using `turboSETI` with the parameters outlined in Table 2.1, a Doppler drift search was carried out on the observed candidates listed in Table 2.3 and 2.4 at both stations. This resulted in the list of ‘hits’ collected in Tables 2.3 and 2.4, where hits are defined as a narrow-band signal detected above the given threshold, $S/N = 10$. The distribution of narrow-band signals detected at both stations is shown in

⁶<https://github.com/gajjarv/BaryCentricCorrection>

TIC ID	Topocentric Results			Barycentric Results		
	LOFAR-SE Hits	I-LOFAR Hits	Mutual Hits	LOFAR-SE Hits	I-LOFAR Hits	Mutual Hits
121966220	387	178	18	376	171	0
249862365	340	193	22	330	196	0
250724252	276	190	21	265	262	0
27677846	313	159	20	294	151	0
470315428	384	175	17	356	224	0

Table 2.2: Comparison of the number of narrow-band signals detected for a subset of *TESS* objects in both the topocentric and barycentric reference frame. `turboSETI` searches were completed using identical parameters in each reference frame. A small number of mutual hits were found in the topocentric frame, but these were filtered out entirely in the barycentric case.

Figure 2.6. A large percentage of hits are seen at both sites in the 120 - 140 MHz range. This falls within the range of expected RFI leakage seen from neighboring airports⁷.

Using a drift-rate search of ± 4 Hz/s for this study covers a fraction of the possible drift rates of transmitters from exotic objects that can be detected as outlined by [Sheikh et al. \(2019\)](#). [Li et al. \(2022\)](#) shows that 4 Hz/s is comprehensive in relative to the expected distribution of exoplanet drift rates. The omission of a search in this parameter space is due to its computationally intense nature of searching for narrow-band signals across a sizeable drift-rate range. However, in doing this, the parameter space searched for ETI signal has been drastically reduced. Continual development of search algorithms like `turboSETI` is progressing to make larger drift-rates searches a more computationally feasible.

Upon first inspection of Figure 2.6 it appears that the results at both stations are somewhat similar. However, upon performing a Kolmogorov-Smirnov (KS) test for each set of results for drift-rate, SN and frequency of detected hits the highest p -value returned was on the order of 10^{-11} indicating that the RFI environments at each of the stations are significantly different.

2.3.3 Dual-site coincidence rejection

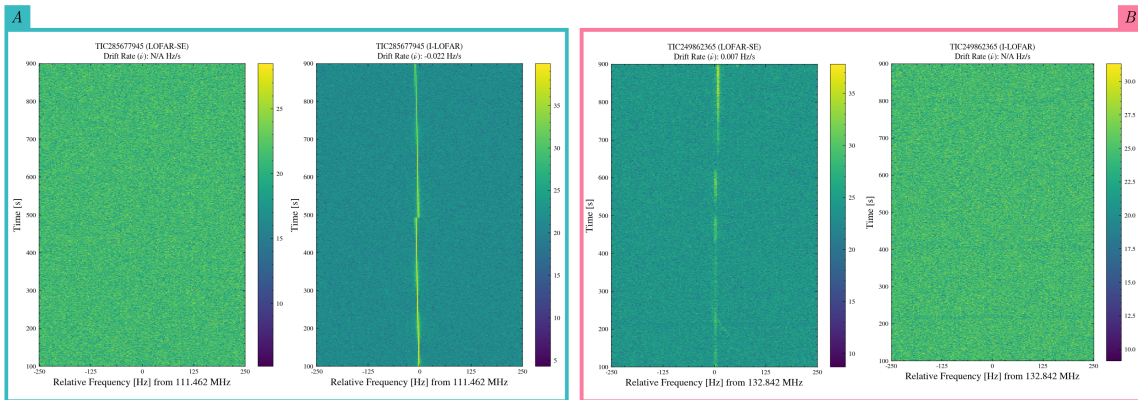


Figure 2.8: Dynamic spectra (waterfall plots) of detected narrow-band signal centered on the detected frequency of detection, showing the two most common cases of coincidence rejection. Case A (*left*) shows a narrowband signal with a non-zero drift rate detected at I-LOFAR and not LOFAR-SE. Case B (*Right*) shows the opposite where a non-zero drift rate signal is not detected by I-LOFAR but is detected by LOFAR-SE. For a signal to be considered a detection of interest both sites would have to exhibit non-zero drift rate signal at the same frequency simultaneously.

In the case of this study, a singular beam observes a single target for 15 minutes at both stations and observations are converted to barycentric reference frame. Narrow-band searches are then performed at

⁷Shannon & Goteborg Landvetter

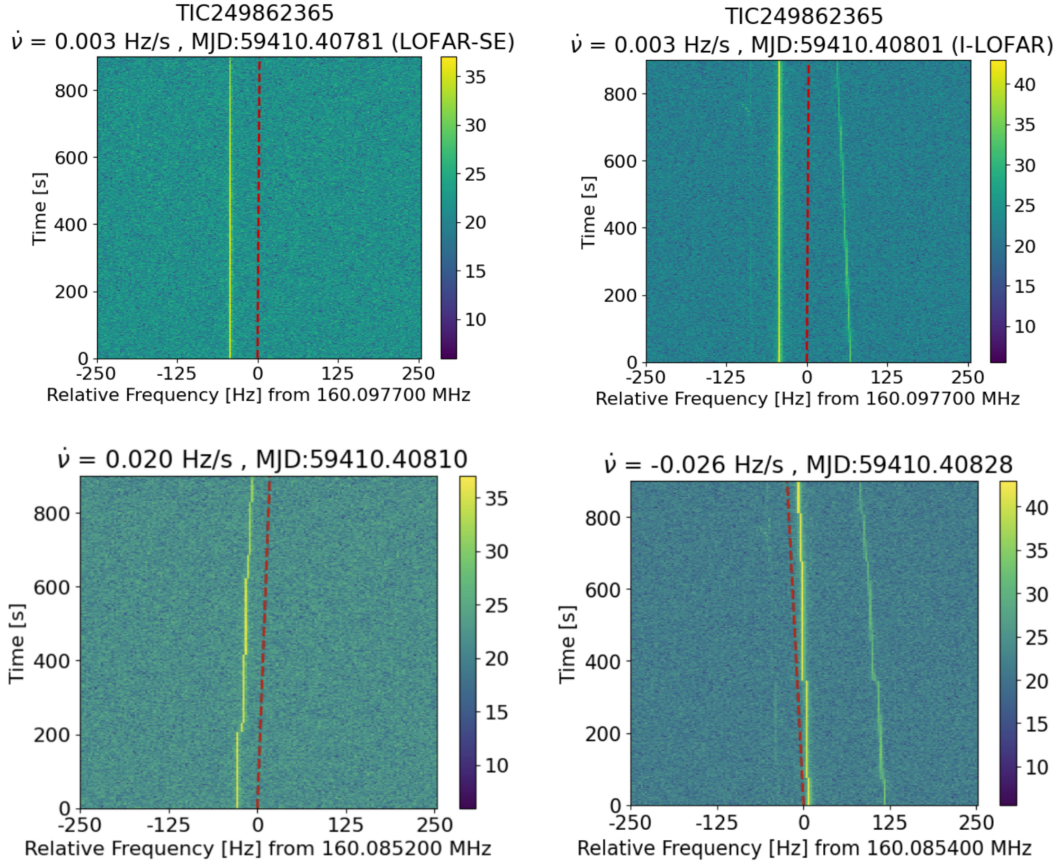


Figure 2.9: The *top* two plots represent narrowband signals detected at both stations in the topocentric frame of reference. The *bottom* two plots show the same detected narrowband signals detected at both stations but corrected to the barycentric frame of reference. This is illustrated by the newly added drift to signals present in the post correction.

both sites, and the results of both searches are compared. In Figure 2.8 two common detection cases are shown and how the use of dual site observation aids in the nature of each signals origin.

Case A: In this case a hit has been detected at the Irish station but is absent from the same frequency at the Swedish station. Thus the signal is rejected as a extraterrestrial emitter and deemed as RFI local to the Irish station.

Case B: Similar to case A but this time the converse is seen, a hit has been detected at Swedish station and not at a the frequency at the Irish station.

In our analysis, a signal is classified as a mutual extraterrestrial hit only if two conditions are met: *a)* the signals are within a frequency range of ± 4 Hz of each other in the barycentric reference frame, and *b)* their drift rates are within ± 0.2 Hz/s of each other after barycentric drift corrections. In Figure 2.9, an intriguing candidate is depicted. In the topocentric frame, we detected a narrowband signal at 160 MHz that was simultaneously present at both stations. However, when converting to the barycentric reference frame (as illustrated in Figure 2.9), the signal appears to be seen at different frequencies with opposite signs due to the different line-of-sight velocities towards the target. As a result, this narrowband signal is rejected as a genuine sky-bound signal.

2.3.4 Search Results

Figure 2.7 depicts the observed drift rates as a function of frequency. As shown in Figure 2.6, a substantial number of hits are observed at 125 MHz and 138 MHz, suggesting the presence of potential aircraft communications within these frequency bands. Notably, at I-LOFAR, a significant number of hits are

also detected at 167 MHz, which is suspected to be related to aircraft communication. Additionally, a pronounced spike in RFI at 164 MHz is observed at the Swedish station (LOFAR-SE), likely associated with marine communications due to the proximity of LOFAR-SE to the coast.

Implementing barycentric corrections and coincidence rejections, no signals of interest were identified among the observed candidates. Comprehensive information regarding the targets and their corresponding hits for both *TESS* and *Gaia* can be found in the supplementary databases presented in the Tables 2.3 and 2.4.

Table 2.3: *TESS* candidates used as bore sight pointings for the survey. These targets were selected from the NASA Exoplanet Archive (NEA) based on visibility at both LOFAR stations.

TIC ID	MJD Start	RA (h)	DEC (°)	Dist. (pc)	LOFAR-SE	I-LOFAR	Mutual
27 677 846	59 410.3856	4.424 676	46.365 902	78.71 ± 0.33	294	151	0
51 024 887	59 410.3189	2.810 346	62.189 260	41.53 ± 0.16	265	181	0
81 831 095	59 410.3300	3.187 109	61.762 385	399.40 ± 5.30	277	196	0
121 966 220	59 410.3967	5.053 188	41.785 784	472.70 ± 9.13	376	171	0
142 090 065	59 402.4266	5.271 567	79.737 727	182.91 ± 1.29	290	282	0
191 146 556	59 410.4078	0.553 625	46.340 305	282.83 ± 3.01	378	266	0
249 862 365	59 410.3078	2.541 534	52.704 091	184.69 ± 1.29	330	197	0
250 724 252	59 410.2967	2.233 683	53.121 508	N/A	265	262	0
266 500 992	59 410.3634	4.078 149	52.256 992	165.31 ± 0.99	276	164	0
288 132 261	59 403.5613	13.965 621	79.583 322	154.94 ± 0.52	328	310	0

Note: First 10 entries shown. Full table available in the supplementary material. Distances are based on Gaia DR2 parallax and uncertainties are from ?. Asterisks denote confirmed NEA exoplanets.

Table 2.4: *Gaia* candidates found within 1.295° of *TESS* boresight pointings. The *Gaia* target pool is drawn from GDR3. Filtering was applied based on parallax error; targets with distance errors $> 20\%$ were excluded to preserve EIRP sensitivity.

Gaia ID	RA (°)	DEC (°)	Dist. (pc)	Teff (K)	Separation (°)	TIC ID	LOFAR-SE	I-LOFAR	Mut
540 394 404 387 737 000	0.003 867	77.7984	850.636	4954.0	1.129	407 394 748	257	181	0
540 420 788 369 495 000	0.008 171	77.9843	836.863	5387.3	1.093	407 394 748	257	181	0
540 290 637 978 301 000	0.011 819	77.5007	563.690	4686.4	1.013	407 394 748	257	181	0
540 431 753 423 271 000	0.017 921	78.2404	1293.320	5365.0	1.295	407 394 748	257	181	0
540 422 957 330 267 000	0.018 887	78.0603	722.054	5415.4	0.958	407 394 748	257	181	0
564 460 068 219 877 000	0.018 908	78.4901	1415.490	5276.0	1.189	407 394 748	257	181	0
540 394 400 090 438 000	0.020 346	77.7933	861.226	5896.3	1.118	407 394 748	257	181	0
540 387 257 562 774 000	0.021 907	77.6559	818.213	4952.0	0.947	407 394 748	257	181	0
564 451 272 126 871 000	0.022 257	78.3080	854.196	4731.2	1.089	407 394 748	257	181	0
540 291 153 374 376 000	0.022 550	77.5313	1105.790	4892.0	0.985	407 394 748	257	181	0

Note: First 10 entries shown. Full table is available in the paper's supplementary material. The table includes each *Gaia* target near a *TESS* pointing and its angular separation from the LOFAR beam boresight.

2.4 Discussion

2.4.1 Survey Sensitivity

The required power for a certain extra terrestrial intelligent (ETI) transmitter to be detected depends on its directionality and other signal characteristics. We can measure the transmitter power of an ETI beacon in terms of the effective isotropic radiated power (EIRP; ?) as,

$$\text{EIRP} = \sigma \times 4\pi d_\star^2 \frac{\text{SEFD}}{\delta\nu_t} \sqrt{\frac{\delta\nu}{n_p t_{obs}}} \text{ W} \quad (2.4.1)$$

Here, σ is the required S/N, $\delta\nu$ is the bandwidth of the received signal, $\delta\nu_t$ is the transmitted bandwidth, t_{obs} is the observing integration time, SEFD is the System Equivalent Flux Density, n_p is the number of polarizations, and d_\star is the distance between the transmitter and the receiver, i.e., the distance to the star. We considered $\delta\nu_t$ to be 1 Hz. For the narrowband signals we consider in our Doppler searches, we assume $\delta\nu$ is matched to our spectral resolution and further assume a temporal duty cycle of 100%.

The SEFD of the international HBA stations used in this survey is on average ~ 900 Jy for most of the band, rising to ~ 1.2 kJy at the band edges (?). For reference, the SEFD of the GBT at the 1.4 GHz is around 10 Jy. This difference in sensitivity is because sky temperature scales as $\nu^{-2.6}$ meaning it can

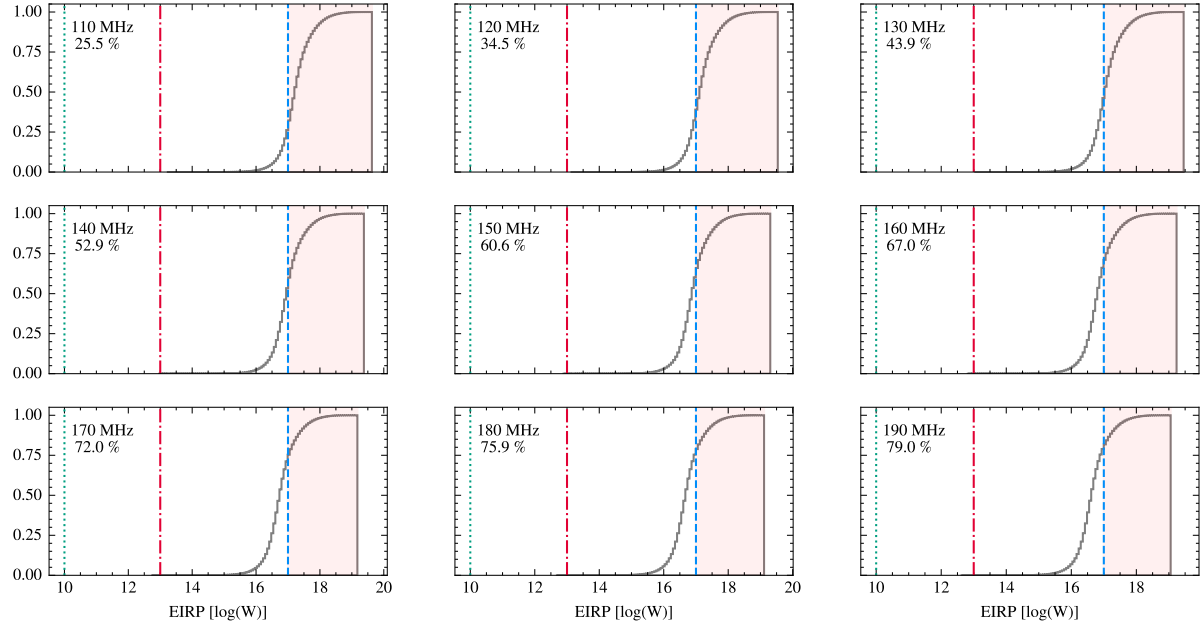


Figure 2.10: Cumulative histogram of EIRP limits of this survey across the HBA band. Reference luminosities for three civilization levels emitting 10^{17} , 10^{13} or 10^{10} W are shown in blue, red and green respectively. The percentage of targets where the station is sensitive to the transmission of 10^{17} W is shown, as a function of frequency across the band. At lower frequencies sensitivity to 10^{17} emitters drops off as the T_{sys} rises. The \bar{T}_{sys} varies from 1260 K down to 322 K as frequency is increased across the band. Detailed calculations are presented in Appendix B.

be hundreds of times higher in the LOFAR band. However, the average values are of little use as there is also a large degree of variation in the sky temperature across the sky. For this reason, we perform a separate calculation for every target to determine the relevant luminosity limit in each case. For example, the sensitivity to each off-boresight target is determined by its proximity to the pointing coordinates. Figure 2.4 depicts both the impact on sensitivity and the number of background stars within a given LOFAR beam. Figure 2.2 shows an example pointing from the survey and also well illustrates the vast volume of targets that appear in a LOFAR beam (pink).

Figure 2.10 presents the luminosity limits for the cumulative targets of this survey within the frequency range of 110 – 190 MHz. In this figure, the limiting luminosity is compared to notable values of Equivalent Isotropic Radiated Power (EIRP) for various scenarios. These scenarios include a Kardashev I type advanced civilization transmitting at a power level of 10^{17} W, an advanced civilization producing planetary radar-level transmissions with a transmitting power of 10^{13} W, and a cumulative aircraft radar-type system transmitted across a large solid angle with a power of 10^{10} W (Siemion et al., 2013). The Figure demonstrates that due to the varying system temperature (T_{sys}) across the frequency band, our observations were sensitive to detecting a range of Kardashev I type targets. Specifically, we were able to detect approximately 25% of the targets at the lower end of the frequency band, increasing to nearly 80% of the targets at the higher end of the band.

2.4.2 Starlink Interference

A recent study by ? has shown that unintended electromagnetic radiation (UEMR) from the Starlink satellite constellation produced broadband interference ranging from 0.1 to 10 Jy and narrowband interference ranging from 10 to 500 Jy. UEMR was detected at frequencies at 110 to 188 MHz, which is the bandwidth of the HBA used in this study. UEMR has many potential consequences for low frequency radio observations. Analysis of turboSETI hit detection's within 1 MHz the UEMR narrowband emission frequencies (125, 135, 143, 150, 175 MHz; ?) show that 17.8% of total detected hits are within this region. This region occupies 18.5% of this study's bandwidth. This result is expected, as UEMR affects a number of different types of radio searches, it does not affect narrowband searches of this nature. This is due to two factors. Firstly satellites in Low Earth Orbit (LEO) to Geostationary orbit (GEO) usually

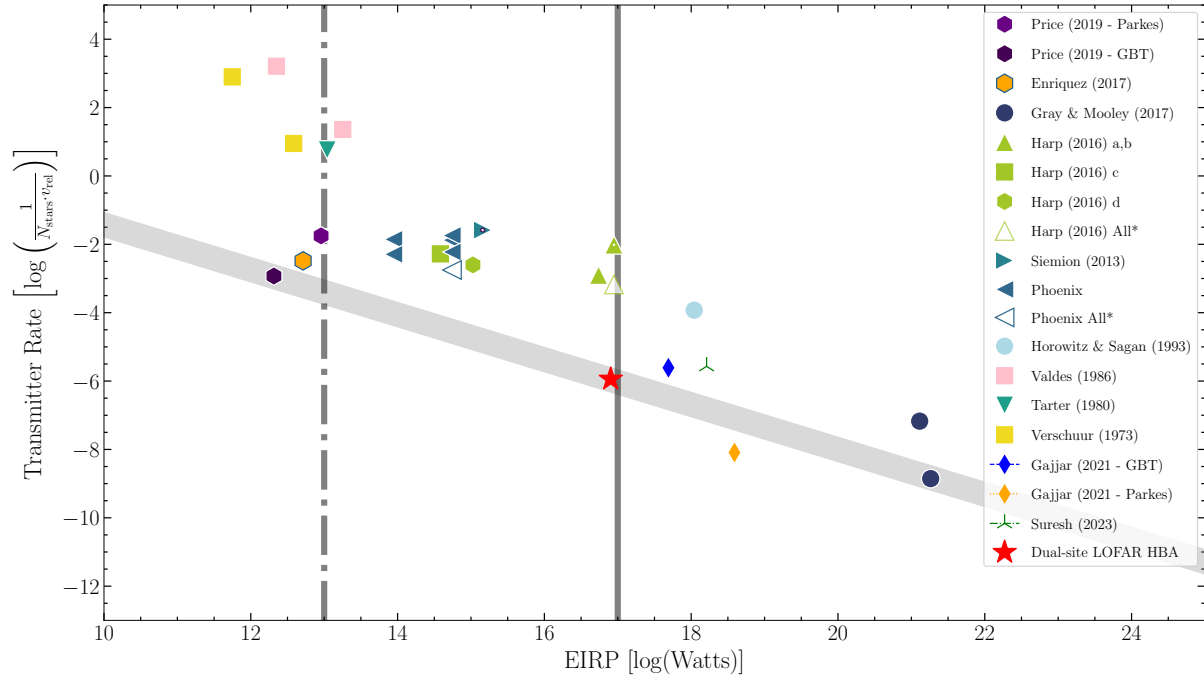


Figure 2.11: Comparison of our study (highlighted in red) to prior surveys. The plot presents the transmitter rate versus Effective Isotropic Radiated Power (EIRP), with the grey line indicating the transmitter rate as a function of EIRP. A solid vertical grey line illustrates the energy surplus of a Kardashev Type-I civilization. Additionally, a dotted-dashed grey line depicts the EIRP of the Arecibo planetary radar. The gray thick line shows the slope of the transmitter-rate as a function of their EIRP power. Distance used for EIRP calculation is $\bar{d} + d_\sigma = 7009$ ly.

have velocities that are too high for them to be detected with the temporal resolution of our data, and they are at drift rate values outside the parameters of this search (>4 Hz/s). Secondly, the satellites are in the near field of each station's beam and due to their relative distance to the observer compared to the bore sight target a satellite less likely to appear in both beams simultaneously. It is concluded that the Starlink constellation does not add to the number of narrowband hits detected in this study.

2.4.3 Figure of Merit

To compare SETI surveys, ? introduced a figure of merit known as the Continuous Waveform Transmitter Rate (CWTMR),

$$\text{CWTMR} = \zeta_{\text{AO}} \frac{\text{EIRP}}{N_{\text{stars}} \nu_{\text{rel}}} \quad (2.4.2)$$

Where N_{stars} is the number of stars in each pointing for a given survey, ν_{rel} is the fractional bandwidth of the survey, $\Delta\nu_{\text{tot}}/\nu_{\text{mid}}$ where ν_{mid} is the central frequency of the survey. ζ_{AO} is the normalization factor such that CWTMR = 1 and the EIRP is equal to the Arecibo radio telescope's S-band planetary radar, if it were transmitted across a whole hemisphere, ($\sim 10^{13}$ W Siemion et al. 2013). In Figure 2.11, we compare our results to those from some other SETI surveys. As this survey continues, the transmitter rate will decrease with the volume of stars observed (N_{stars}), as outlined by Equation (2.4.3).

$$\text{Transmitter Rate} = \log \left[\frac{1}{N_{\text{stars}} \cdot \nu_{\text{rel}}} \right] \quad (2.4.3)$$

As dictated by Equation (2.4.1) to be sensitive to lower powered ETI transmitters, the observation sensitivity needs to be greater. This can be done by employing further LOFAR stations for n -site simultaneous observations through coherent summation.

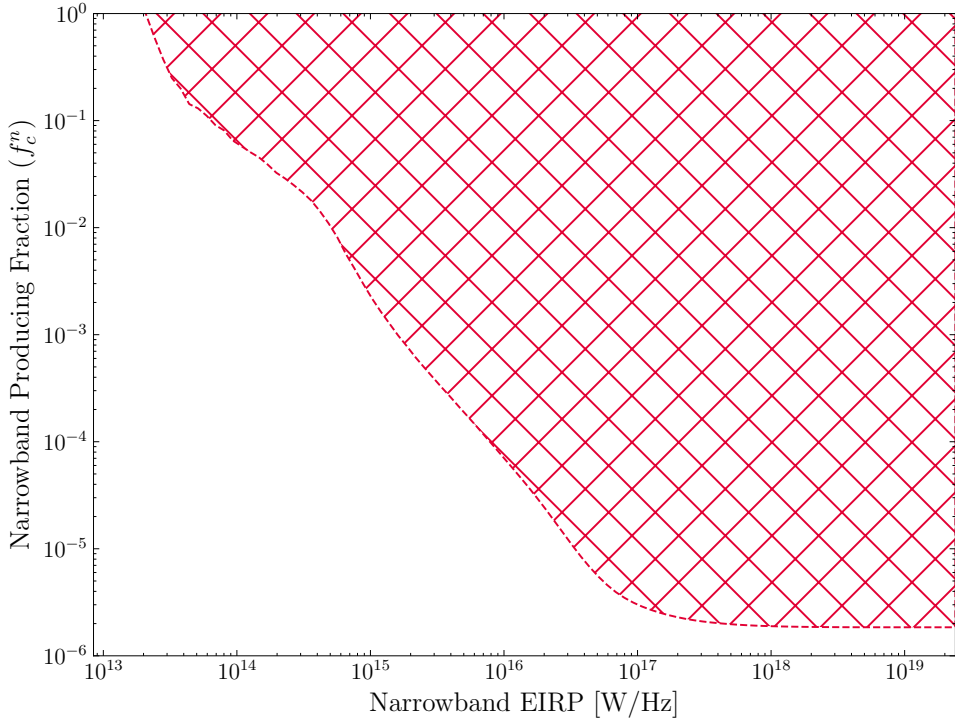


Figure 2.12: The fraction of stars that produce narrow-band emission (f_c^n) against the transmitter power of the total target pool. The hashed region (red) shows the constraints this survey places on a value of f_c^n at 110 - 190 MHz.

2.4.4 110 - 190 MHz Technosignature Parameter Space

The number of intelligent civilizations is quantified using Equation (2.4.4), coined by ?.

$$N = R_* f_p N_e f_l f_i f_c L \quad (2.4.4)$$

In this expression N is the number of communicative civilizations in the Milky Way galaxy, R_* is the rate of star formation per year in the galaxy, f_p is the fraction of stars that have planets around them, n_e is the average number of planets that can potentially support life per star that has planets, f_l is the fraction of potentially life-supporting planets that actually develop life, f_i is the fraction of planets with life that go on to develop intelligent life and f_c is the fraction of civilizations that develop a technology that releases detectable signs of their existence into space.

In Gajjar et al. (2022) a modified variation of the Drake equation (Equation. (2.4.5); Shklovskii and Sagan 1966) is used to constrain the fraction of narrowband emitting civilizations (f_c^n).

$$N = R_{\text{IP}} f_c^n L \quad (2.4.5)$$

Here R_{IP} is defined as the emergence rate (yr^{-1}) of intelligent life in the Milky Way. Figure 2.12 shows the constraint that this survey places on f_c^n when using a Poisson sided upper limit at 95% confidence which in this case is 2.995 as per Gehrels (1986). This provides the most stringent constraint of f_c^n in this frequency range.

2.4.5 Future work using LOFAR 2.0

LOFAR is soon to undergo a staged series of upgrades across all stations in the array. These upgrades at individual stations across Europe will involve the installation of a new Receiver Control Unit (RCU) as described in ASTRON (2023). These RCUs will enable the simultaneous use of both the LBA and HBA in the frequency range of 15 - 240 MHz. This enhancement will allow for a SETI survey across a broader low-frequency band.

Specifically, at 30 MHz, the FWHM will cover an area of 19.39 deg^2 , decreasing to 1.73 deg^2 at 190 MHz. This will enable follow-up LOFAR surveys to encompass a larger volume of stars and a broader frequency domain.

2.5 Conclusion

This paper presents a SETI search in a mostly unexplored parameter space as seen with other SETI surveys (??) by simultaneously observing TESS and Gaia targets of interest in the 110 – 190 MHz radio window. It also demonstrates dual-site coincidence rejection showing that it provides a new method to discriminate candidate extra-terrestrial signals from terrestrial radio frequency interference. We propose this method as a promising means of follow-up for confirmation of any candidates interest arising in this type of study or others in this frequency range. Each target within our fields was then searched for narrow-band signals at each station using our most up to date search techniques (?). The benefit of barycentric correction for eliminating false positives is also demonstrated. Finally the first stringent constraints on the fraction of transmitting civilizations at this frequency range have been shown further constraining the parameter space the Drake equation presents.

As the LOFAR SETI observation campaign continues and more high resolution frequency data is collected, a machine learning search method comparable to ? can be trained and implemented to seek out signals of interest. Multiple LOFAR stations, or indeed sub-arrays of any other wide-footprint radio array allows the option for a coincidence rejection method over the ‘ON’ and ‘OFF’ beam pointings used previously. For future low-frequency SETI surveys, the use of further international stations and a prolonged observation campaign will place even further constraints on an ETI residing in this parameter space. The addition of one or more LOFAR stations would allow for the use of localising a signal of interest in the u-v plane which would be useful for follow up observations. This would be done post-facto through correlation of saved voltages for any candidates of interest.

Bibliography

ASTRON (2023). Lofar2.0 white paper - v2023.1.

Gajjar, V., LeDuc, D., Chen, J., Siemion, A. P. V., Sheikh, S. Z., Brzycki, B., Croft, S., Czech, D., DeBoer, D., DeMarines, J., Drew, J., Isaacson, H., Lacki, B. C., Lebofsky, M., MacMahon, D. H. E., Ng, C., de Pater, I., Perez, K. I., Price, D. C., Suresh, A., Webb, C., and Worden, S. P. (2022). Searching for Broadband Pulsed Beacons from 1883 Stars Using Neural Networks. *ApJ*, 932(2):81.

Gehrels, N. (1986). Confidence Limits for Small Numbers of Events in Astrophysical Data. *ApJ*, 303:336.

Ginsburg, A., Sipőcz, B. M., Brasseur, C. E., Cowperthwaite, P. S., Craig, M. W., Deil, C., Guillochon, J., Guzman, G., Liedtke, S., Lian Lim, P., Lockhart, K. E., Mommert, M., Morris, B. M., Norman, H., Parikh, M., Persson, M. V., Robitaille, T. P., Segovia, J.-C., Singer, L. P., Tollerud, E. J., de Val-Borro, M., Valtchanov, I., Woillez, J., The Astroquery collaboration, and a subset of the astropy collaboration (2019). astroquery: An Astronomical Web-querying Package in Python. *The Astronomical Journal*, 157:98.

Lebofsky, M., Croft, S., Siemion, A. P. V., Price, D. C., Enriquez, J. E., Isaacson, H., MacMahon, D. H. E., Anderson, D., Brzycki, B., Cobb, J., Czech, D., DeBoer, D., DeMarines, J., Drew, J., Foster, G., Gajjar, V., Gizani, N., Hellbourg, G., Korpela, E. J., Lacki, B., Sheikh, S., Werthimer, D., Worden, P., Yu, A., and Zhang, Y. G. (2019). The Breakthrough Listen Search for Intelligent Life: Public Data, Formats, Reduction, and Archiving. *PASP*, 131(1006):124505.

Li, J.-K., Zhao, H.-C., Tao, Z.-Z., Zhang, T.-J., and Xiao-Hui, S. (2022). Drift Rates of Narrowband Signals in Long-term SETI Observations for Exoplanets. *The Astrophysical Journal*, 938(1):1.

McKenna, D. J., Keane, E. F., Gallagher, P. T., and McAuley, J. (2023). udpPacketManager: An International LOFAR Station Data (Pre-)Processor. *The Journal of Open Source Software*.

Sheikh, S. Z., Wright, J. T., Siemion, A., and Enriquez, J. E. (2019). Choosing a maximum drift rate in a seti search: Astrophysical considerations. *The Astrophysical Journal*, 884(1):14.

Shklovskii, I. S. and Sagan, C. (1966). *Intelligent life in the universe*.

Siemion, A. P. V., Demorest, P., Korpela, E., Maddalena, R. J., Werthimer, D., Cobb, J., Howard, A. W., Langston, G., Lebofsky, M., Marcy, G. W., and Tarter, J. (2013). A 1.1-1.9 GHz SETI Survey of the Kepler Field. I. A Search for Narrow-band Emission from Select Targets. *The Astrophysical Journal*, 767:94.

Tarter, J. C. (1996). Project Phoenix: the Australian deployment. In Kingsley, S. A. and Lemarchand, G. A., editors, *Photonics West '96*, pages 24–34. SPIE.

Wlodarczyk-Sroka, B. S., Garrett, M. A., and Siemion, A. P. V. (2020). Extending the Breakthrough Listen nearby star survey to other stellar objects in the field. *MNRAS*, 498(4):5720–5729.

A | Useful Formula

A.1 Fundamentals

$$\vec{\varepsilon} = (\hat{a}\varepsilon_a + \hat{b}\varepsilon_b) \exp(2\pi i(ft - kt)) \quad (\text{A.1.1})$$

A.2 Radiometer

$$T_{\text{sys}} = T_{\text{ant}} + T_{\text{atm}}(1 - e^{-\tau a}) + T_{\text{spill}} + T_{\text{CMB}} + \dots \quad (\text{A.2.1})$$

$$\sigma_{T_{\text{sys}}} = \frac{T_{\text{sys}}}{\sqrt{n_p t \Delta f}} \quad (\text{A.2.2})$$

$$S = \frac{2kT_{\text{sys}}}{A_e} = \frac{T_{\text{sys}}}{G} = \text{S.E.F.D} \quad (\text{A.2.3})$$

$$\sigma_S = \frac{T_{\text{sys}}}{G \sqrt{n_p t \Delta f}} \quad (\text{A.2.4})$$

$$S_{\text{min}} = \frac{\text{SNR} \cdot 4T_{\text{sys}}}{G \sqrt{n_p t \Delta f}} \quad (\text{A.2.5})$$

$$\theta_{\text{HPBW}} \approx 1.2 \frac{\lambda}{D} \quad (\text{A.2.6})$$

A.3 Pulsars

$$\delta = \frac{W}{P} \quad (\text{A.3.1})$$

A.3.1 Spin Down

A.4 Binary Pulsars

A.5 Dispersion Measure

$$\Delta t = 4149 \times \text{DM} \times \left(\frac{1}{f_2} - \frac{1}{f_1} \right) \quad (\text{A.5.1})$$

A.6 Units

Jansky: $10^{-26} \text{ W/m}^2/\text{Hz}$

B | Post-detection Barycentric Correction

We have developed a novel barycentric correction code specifically designed for high-spectral resolution `sigproc` filterbank products for technosignature searches (?). The code uses the TEMPO routine to calculate relative velocity towards the observing targets at both locations, thus allowing for precise correction of the barycentric drift.

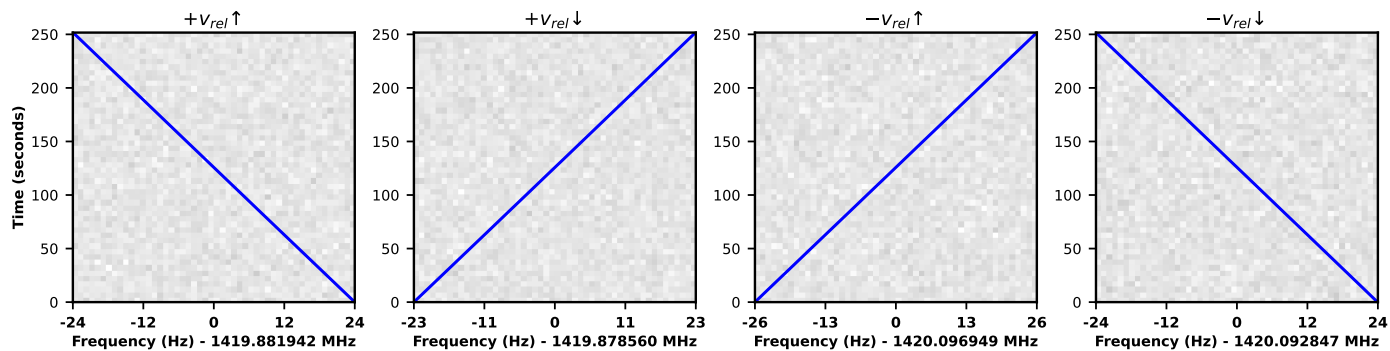


Figure B.1: Doppler drift of a narrowband signal in the topocentric observing frame at four different observing epochs. Simulated waterfalls with narrowband signals observed from the Irish LOFAR station towards the direction of TIC 27677846 are shown for different times of the year in blue. The expected sign and direction of change of the relative velocity are labeled at the top of each plot. It is assumed that a hypothetical narrowband ETI signal is transmitted at a constant frequency of 1420 MHz (with zero drift rate). As shown, the same signal is observed at different frequencies and drift rates depending on the sign and direction of change of the relative velocity at different epochs of observations. For instance, in the first panel, the relative velocity is positive and increases with observing time. Therefore, the observing frequency has been shifted to a lower frequency (as described by Equation 2.3.1), and it continues to shift to even lower frequencies with time.

The Doppler shift caused by the relative motion between the transmitter and receiver will change over time as it is observed. Over a longer time frame, these shifts will exhibit a sinusoidal curve with a sidereal year period. Over a shorter time frame, the same pattern (superimposed on the yearly pattern) will be visible, but with a sidereal day period. Consequently, the relative velocity will change during the observation period, thereby altering the observed frequency of the received narrowband signal. This leads to a drift in the narrowband signal observed by the observer. Figure B.1 displays examples of observed drifts at four different epochs for the same narrowband signal source observed from the same location. It is evident that if the relative velocity is positive and increasing with time (leftmost plot in Figure B.1), the signal, which is stationary in the barycentric frame, will drift towards lower frequencies as time progresses in the topocentric frame, as per Equation 2.3.1.

B.0.1 Algorithm outline

Figure B.2 shows an example of how data is arranged in a filterbank file. For our case, we will assume that in a given filterbank file, frequency channels are in descending order with the first channel (f_1) having the highest frequency for each time sample. The goal of our tool is to shift every frequency channel

from the observing frame to the actual emitted frequency frame after correcting for the barycentric relative velocity to remove any additional narrowband signal drift introduced by it. We aim to keep the first channel frequency of all the time samples the same in the barycentric frame also, thus relative shifts between spectra are needed to apply for each time sample corresponding to the inferred relative velocities. Our tool measures relative velocity at each time sample towards a given direction in the sky from a given telescope at the time of observations. Let's assume an observing scenario where $v_{rel} > 0$. Following Equation 2.3.1, we can state that the emitted frequency (or barycentric frequency) will be higher than the observed frequency. That means that observations stored in the first topocentric frequency channel correspond to higher barycentric frequency. Thus, this spectra needs to be shifted to higher frequency. If the relative velocity increases with time, the consecutive time sample's first channel barycentric frequency will be slightly higher than the previous sample's first channel emitted frequency. Our tool thus shifts the spectra of each time sample towards higher frequency such that the first channel's emitted frequency matches across all time samples. Due to these shifts, we either replace empty channels at the edge of the spectra with zeros in case of squeeze or drop extra channels in case of expansion.

As given in Equation 2.3.1, the Doppler shifts are frequency-dependent, impacting higher frequencies more than lower frequencies. In other words, for spectra where frequencies are ordered from higher to lower frequency, the first channel will be shifted more compared to the last frequency channel. To compensate for this, we either expand or squeeze spectra as shown in Figure B.3. Figure B.4 outlines the logical flow of the code for a case of an input filterbank file with a descending order of frequency. By comparing Figure B.1 and the code outline in Figure B.4, we can consider one of the cases where the relative velocity is negative and increasing in absolute value with time. In this case, we need to shift consecutive spectra to lower and lower frequencies to match up their first frequency channel. Furthermore, for any negative relative velocity (either increasing or decreasing with time), we need to squeeze the individual spectra as shown in Figure B.3. Similarly, the same can be considered for the case of positive relative velocity. The code for this algorithm is publicly available here¹.

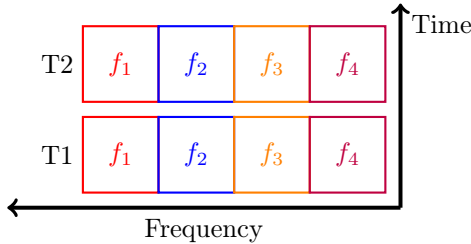


Figure B.2: A typical filterbank file stores data in a time and frequency matrix format. Each row represents a sample, while each column represents a frequency channel for a given sample. Time is increasing from bottom to top while the frequency is increasing from right to left.

B.1 Sensitivity of the Survey across the HBA

As previously stated the high band antenna spans from 110 - 190 MHz. The system temperature across the band significantly, which reduces the sensitivity of LOFAR at the lower end of the band-pass (see. Figure 2.10). Calculation of T_{sys} and consequently SEFD follows a modified method as outlined in § 3.3 of ?. The method differs in the calculation of T_{sky} as this is pointing dependent. This study uses the LWA1 Low Frequency Sky Survey (?) for sensitivity analysis. We calculate system equivalent flux density (SEFD; Jy) as follows,

$$\text{SEFD} = \frac{2T_{sys}k_b}{A_e} \quad (\text{B.1.1})$$

Where k_b is the Boltzmann constant and A_e is the effective collecting area of a single station HBA. EIRP is then consequently calculated using Equation (2.4.1).

¹<https://github.com/gajjarv/BaryCentricCorrection>

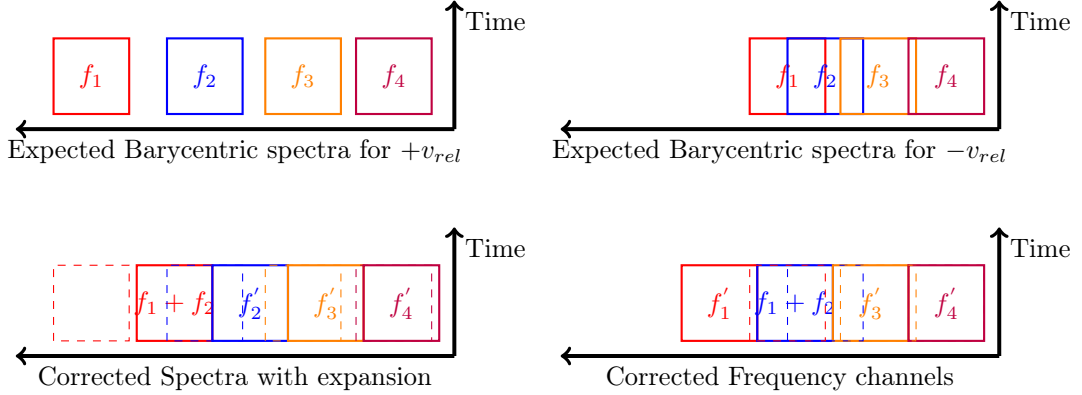


Figure B.3: These plots depict the expected spectra at their respective barycentric frequencies and the spectra after the correction for barycentric relative velocity. Each plot represents a single spectrum, where the frequency increases from right to left. (a) In the case of $+v_{rel}$, the first channel of the topocentric spectra is shifted to a higher barycentric frequency compared to the last topocentric spectra channel, which causes an expansion of the spectra. If two consecutive channels move farther away from each other (shown as f_1 and f_2) by more than half the channel width, an additional channel is added in between, which is the summation of these two channels. Extra channels at the edge of the spectra are dropped. (b) In the case of $-v_{rel}$, the first channel of the topocentric frequency is shifted to a lower barycentric frequency relative to the last topocentric spectra channel, which causes a squeeze in the spectra. If two consecutive frequency channels shift closer to each other by more than half a channel width, these channels are added together and an extra channel is added at the end containing zeros. The bottom spectra in each plot illustrate these expansion and squeeze effects after correction are applied from the code.

Frequency (MHz)	110	120	130	140	150	160	170	180	190
T_{sys} (K)	1305.073	1051.633	862.204	717.304	604.260	514.594	442.408	383.552	335.019
SEFD (Jy)	2148.125	1730.967	1419.171	1180.668	994.601	847.011	728.195	631.320	551.435
EIRP (W)	17.273	17.179	17.092	17.011	16.937	16.866	16.801	16.738	16.679
EIRP _{median} (W)	17.235	17.141	17.054	16.974	16.899	16.829	16.763	16.701	16.642
EIRP _{max} (W)	19.628	19.537	19.454	19.377	19.304	19.237	19.173	19.112	19.055
EIRP _{min} (W)	12.627	12.627	12.627	12.627	12.627	12.627	12.627	12.627	12.627
K1 detectable (%)	25.497	34.493	43.910	52.859	60.644	66.968	71.969	75.887	79.032
Earth detectable (%)	14.659	20.613	27.730	35.694	43.908	51.781	58.826	64.739	69.612

Table B.1: Statistics on sensitivity across the HBA band. The K1 and Earth detectable values represent the percentage of the target sample that are detectable.

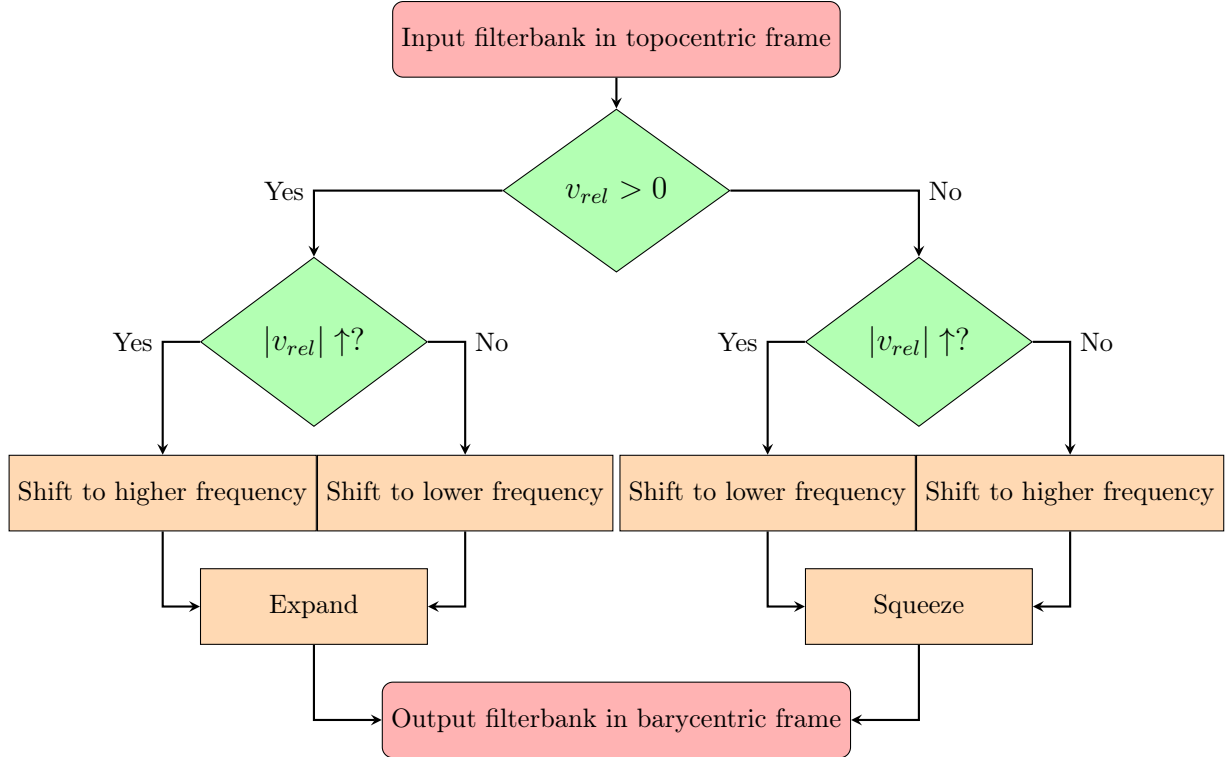


Figure B.4: An outline of the post-detection barycentric correction algorithm for an input filterbank file in `sigproc` format. For this case, the input filterbank file has a descending order in frequency, and v_{rel} represents the relative velocity between the transmitter and observer. The algorithm considers two cases depending on whether the relative velocity is positive or negative, which indicates whether the source is moving away from or towards the observer, respectively. Each of these cases is further divided into two where the absolute value of the relative velocity can either increase or decrease, requiring the spectra to be shifted to either the higher or lower frequency end. For all cases with $+v_{rel}$, each spectra is expanded, and for $-v_{rel}$, each spectra is squeezed, as shown in Figure B.3. The code then writes each of these spectra into another `sigproc` filterbank file, which will have each channel frequency closely corrected to the barycentric frame of reference.